New Q and V-band ECE radiometer for low magnetic field operation on LHD

Tokihiko Tokuzawa[1,2*], *Yuki* Goto[1], *Daisuke* Kuwahara[3], *Masaki* Nishiura[1,4], and *Takashi* Shimizu[1,]

[1]National Institute for Fusion Science, National Institutes of Natural Sciences, Toki 509-5292, Japan
[2]The Graduate University for Advanced Study, SOKENDAI, Toki 509-5292, Japan
[3]College of Engineering, Chubu University, Kasugai 487-8501, Japan
[4]Graduate School of Frontier Sciences, The University of Tokyo, Kashiwa 277-8561, Japan

Abstract. To meet the demand for information on electron temperature fluctuations in low magnetic field experiments in the Large Helical Device (LHD), a new ECE radiometer covering the Q and V bands has been installed. Combination mirrors are installed in the vacuum vessel to focus the beam and efficiently propagate the radiated electron cyclotron waves. Notch filters are used to eliminate stray light from the gyrotron, and a 32-channel heterodyne radiometer is constructed using a filter bank system. As a result, oscillations of electron temperature and both electromagnetic and electrostatic fluctuations were successfully observed.

1 Introduction

~~The e~~Electron cyclotron emission (ECE) measurements have been applied to electron temperature measurements in many torus plasma devices confined by magnetic fields. The Large Helical Device (LHD) [1, 2] has been equipped with three types of ECE measurement system (Michelson interferometer, grating polychromator (GPC), and radiometer) to provide electron temperature information since the beginning of the experiment (1998). [3-11]. Recently, plasma fluctuations (such as L-H transitions and MHD bursts, etc.) at a low magnetic field around B_t =1 – 1.375 T have attracted attention at LHD [12-15]. ~~however~~However, the existing ECE radiometers cover frequencies from 50 –150 GHz and are optimized especially for the high frequency range above 100 GHz. ~~In~~ At this time, we have developed an ECE radiometer for such low magnetic field strength experiments.

Figure 1 shows the spatial distribution of the characteristic frequency at the LHD horizontal port when the on-axis toroidal field strength (B_t) is 1T. Unlike the tokamak, the LHD magnetic field strength distribution has a hill-shape, which allows observation from the outer port in the outer half of the region from the plasma magnetic axis. As shown in Figure 1(b), the extraordinary mode (X-mode) ~~2nd~~ second harmonic EC wave satisfies the optical depth of $\tau > 1$ in the entire plasma region. Since the EC waves in the core region are optically thin but overlap with the third harmonic waves in the periphery, the system was designed with $0.3 < \rho < 1.0$, as the measurement region at this magnetic field configuration, in which the magnetic axis position in the vacuum field R_{ax} = 3.60 m, the helical coil pitch parameter γ = 1.2538, and the ratio of the quadrature field B_q = 100 %.

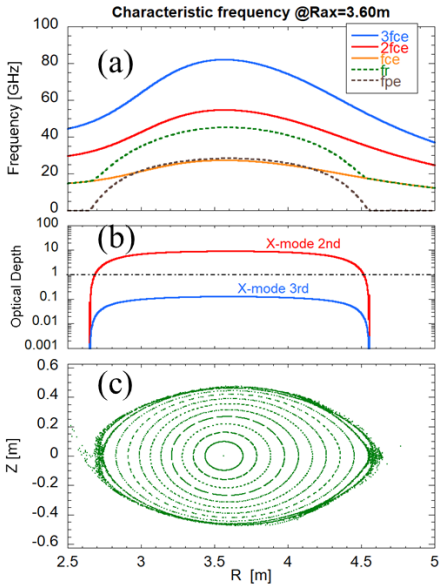

Fig. 1. (a) Radi~~d~~al profile of characteristic frequencies in the major radial direction in the LHD horizontal cross section at B_t =1T and R_{ax} =3.60m. The blue line is the ~~third~~ 3rd harmonic $3f_{ce}$, the red line is the 2nd harmonic $2f_{ce}$, the yellow line is the fundamental f_{ce}, the green dotted line is the right-hand X-mode cutoff frequency, and the brown dotted line is the electron plasma frequency f_{pe}. Here the electron density is calculated as n_{e0}=1x10^{19} m^{-3} at the center. (b) Optical thickness at T_e = 2 keV, where the X-mode 2nd harmonic f_{ce} exceeds 1 almost everywhere in the plasma confinement region. (c) Closed flux surface per ρ = 0.1 and ergodhic region in vacuum.

* Corresponding author: tokuzawa@nifs.ac.jp

This paper describes the diagnostic system, including the focusing optics and heterodyne radiometer circuit, in Chapter 2, and preliminary plasma experimental results in Chapter 3.

2 Experimental arrangements of ECE

In the application of the ECE radiometer for this low magnetic field experiment, the system was required to efficiently receive EC waves from the plasma and to detect the received signals with high temporal and spatial resolution. The details of the developed system for each of these items are described below.

2.1 In-vessel optical mirrors

The LHD has a complicated vacuum vessel structure for cooling the superconducting coils, and the distance between the port and the plasma is far, as shown in Figure 2. Since it is also difficult to prepare a large vacuum window, we considered installing a focusing optics system inside the vacuum vessel. For this purpose, two aluminium mirrors are used in combination. One mirror (M1) is a concave mirror (500 x 350 mm, focal length of 600 mm) and the other (M2) is a plane mirror (350 x 250 mm). To transmit the EC wave from the plasma to the receiver antenna with these mirrors, the beam width at the vacuum window must be narrowed down to 150 mm or less. The beam radius ω at each position is obtained from the following Gaussian beam propagation equation,

$$\omega(z) = \omega_0 \sqrt{1 + \left(\frac{\lambda z}{\pi \omega_0^2}\right)^2} \qquad (1)$$

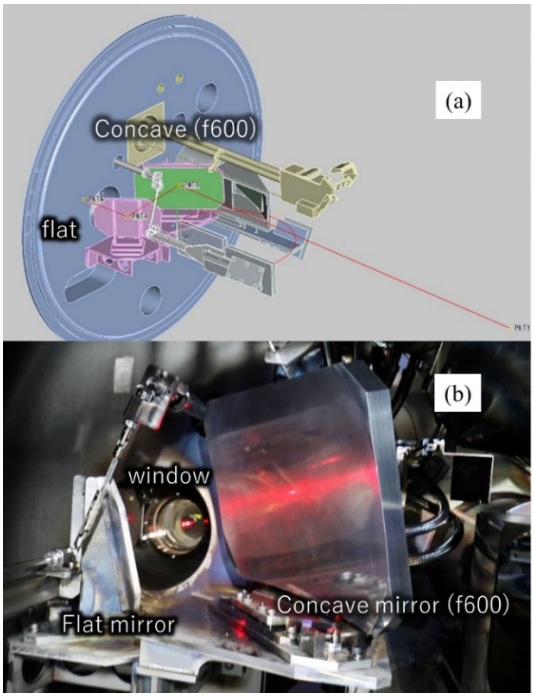

Fig. 4. (a) CAD design and (b) photograph of combination mirrors in LHD vacuum vessel.

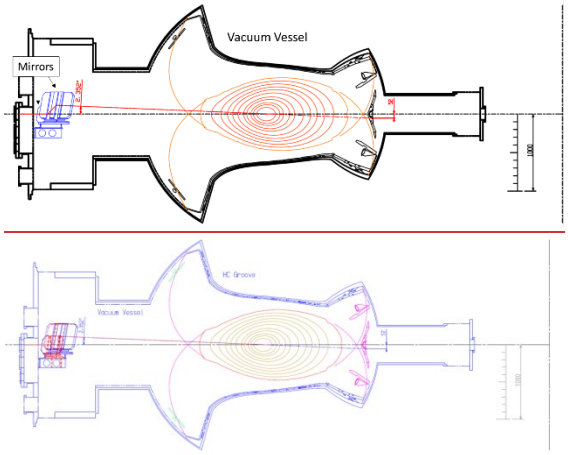

Fig. 2. Cross-sectional view inside the LHD 9-O port vacuum vessel, with two mirrors to focus the beam at the plasma center; the distance from M1 to the plasma center is around 2.5 m. The EC waves are detected at an angle of 2.3 degrees, with the line of sight looking slightly upward from the horizontal plane.

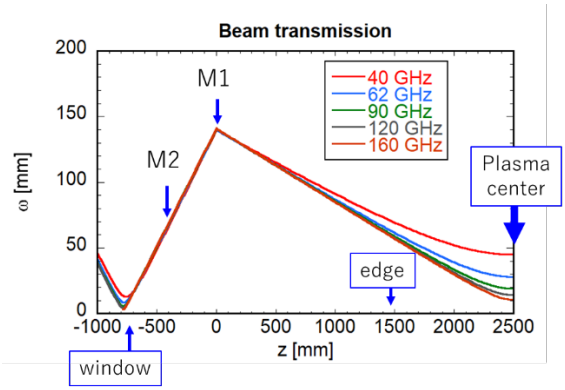

Fig. 3. Beam size evolution at each position, determined by Gaussian beam propagation theory. z = 0 for the position of M1.

and is shown in Figure 3. Here, λ, ω_0 are the wavelength and the beam radius at the beam waist, respectively. z is defined as the distance to the location of the beam waist, and the location of the mirror M1 is set as the reference point~~from the M1 mirror~~. This optical system is expected to have a beam width of 40 mm at 40 GHz, 28 mm at 62 GHz, and 10 mm at 160 GHz at the plasma centre. In the vacuum vessel, the two mirrors are placed in the arrangement shown in Figure 4. To avoid interference with existing equipment, the M1 mirror was placed slightly (115 mm) above the horizontal plane in the vertical direction. However, the change in pitch angle was slight and the field of view was sufficient, so there were no problems with ECE measurements. A shutter wa~~i~~s also installed on the vacuum windows to protect them from dirt during wall conditioning.

To evaluate the performance of the focusing optics, we placed a millimeter-wave source at the position of the vacuum window and investigated the beam propagation characteristics. For example, as shown in Figure 5, the beam radius at 1.5 m from the M1 mirror is 79 mm for the 39 GHz millimeter wave and 67 mm for the 150 GHz. These results are in good agreement

with the calculated values from Gaussian beam propagation.

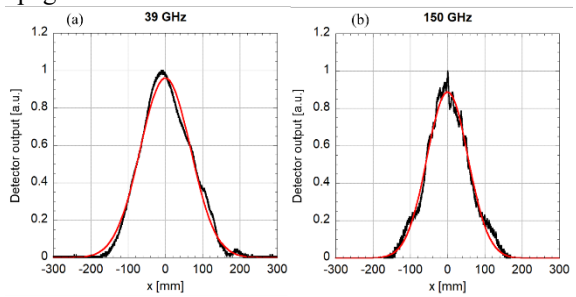

Fig. 5. Beam profiles at 1.5 m from the M1 mirror for (a) 39 GHz and (b) 150 GHz millimeter waves. Black lines are measurements, red lines are Gaussian fits. Intensities are normalized to the maximum of the measured values.

2.2 Heterodyne Radiometer system

A Q-band and V-band heterodyne radiometer system has been developed. The system consists of two sections which are the radiofrequency (RF) section and the intermediate frequency (IF) ~~section~~ one in each frequency band.

2.2.1 RF section

As shown in Figure 6, two bands, Q-band and V-band, were constructed. The EC waves are transmitted through a 2.5-inch corrugated waveguide at a distance of approximately 12 meters from the receiving antenna. After each band is divided and amplified by a low-noise amplifier (LNA) with a gain of 30 dB, the ECE waves are led to a mixer and detected in each band. Both systems use a low-noise DSO oscillator as the local (LO) source for high-sensitivity heterodyne detection, which is multiplied and input to the mixer. The IF signal at the mixer output is amplified by an IF amplifier and led into the next IF section.

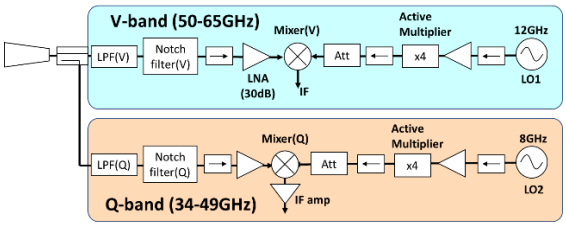

Fig. 6. System schematic of heterodyne radiometer RF section. LPF, LNA, and Att represent a low-pass filter, a low-noise amplifier, and an attenuator, respectively. The LO frequencies of the mixer are 48 GHz and 32 GHz for V-band and Q-band, respectively.

56 GHz and 77 GHz gyrotrons are used as second harmonic ECH for plasma ignition and heating in the experimental condition of the magnetic field strengths near B_t = 1 T. Due to the high-power output of these gyrotrons, it is necessary to eliminate stray light effects that can damage radiometers and cause saturation of mixers and amplifiers. For this reason, we developed a waveguide cavity-type notch filter and the detailed design values for the Q-band case are given in Ref. 16. On the other hand, a V-band notch filter was also fabricated with the design dimensions, as shown in Table 1. Notch filters (NOTCH (A) and NOTCH (B)) were fabricated separately for each gyrotron frequency, and the waveguides were connected in series so that the two frequencies could be excluded. The performance of the combinate notch filter is shown in Figure 7. The attenuation is 80 dB at 56 GHz and 60 dB at 77 GHz, indicating that a notch filter with sufficient performance could be developed.

Table 1. Design parameters for V-band notch filters for 56GHz and 77 GHz.

	NOTCH (A)	NOTCH (B)
Center frequency [GHz]	56.0	77.0
Cavity diameter [mm]	4.12	3.0
Cavith length [mm]	4.546	2.62
Cavity gap length distance between two resonators [mm]	5.726	3.42
Slit width [mm]	0.5	0.5
Slit length [mm]	3.759	1.6
Slit depth [mm]	0.5	0.3

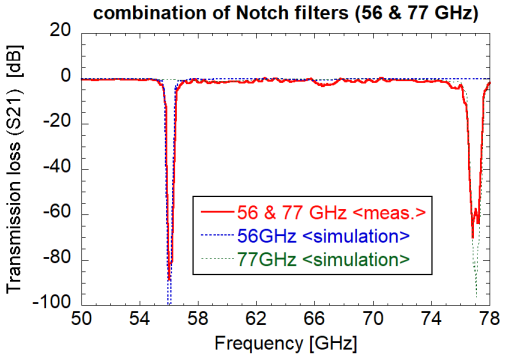

Fig. 7. Frequency response of combined notch filters.

2.2.2 IF section

A schematic diagram of the IF section is shown in Figure 8, where a similar system is used for both Q-~~band~~ and V-band to detect each frequency ECE component. The IF signal at the output of the mixer is divided into two parts, and the 2-9 GHz component is amplified by the LNA and enters the filter bank. There it is separated into eight frequency components, discriminated by a BPF with a bandwidth of 800 MHz (described below), and then detected by the Schottky diode detector. The detector output signal is collected throughout the discharge by an ADC (NI PXIe-6378) with 16-bit

resolution and 1 MS/s sampling rate. On the other hand, the 10-17 GHz component is down converted to 2-9 GHz by Mixer3 using the 19 GHz signal (LO3), because we want to align the characteristics using a similar filter bank set for signal detection~~and signal detection is performed in the similar filter bank~~. Thus, each band has 16 frequency channels each, making a total system of 32 channels.

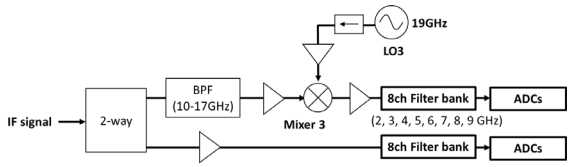

Fig. 8. Schematic diagram of IF section.

In the filter bank, each ECE wave is discriminated by a 2-9 GHz BPF. The bandwidth of all BPFs is designed to be ±400 MHz. The transmission characteristics of the BPFs, measured using a vector network analyser, are shown in Figure 9. It can be seen that each frequency component can be discriminated with the contamination of other frequency components suppressed to -50 dB or more.

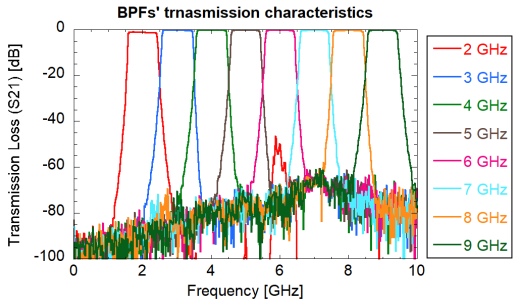

Fig. 9. Frequency response of each bandpass filter.

2.2.3 Integration test

The entire heterodyne radiometer system was then tested with a noise source. Instead of EC wave radiation from the plasma, we examined how the signal output of each frequency component from the filter bank changed when a combination of noise sources and attenuators for each band were placed at the antenna locations in the RF section diagram in Figure 6. The strength of the RF signal input to the mixer (from the noise source) was varied by controlling the attenuator from a squeezed state (-32 dB) to a released state (-1 dB). The detector output obtained at that time is shown in Figure 10. Each channel corresponds to 54-57 GHz frequency components. The detector output was found to vary linearly with respect to the change in RF intensity.

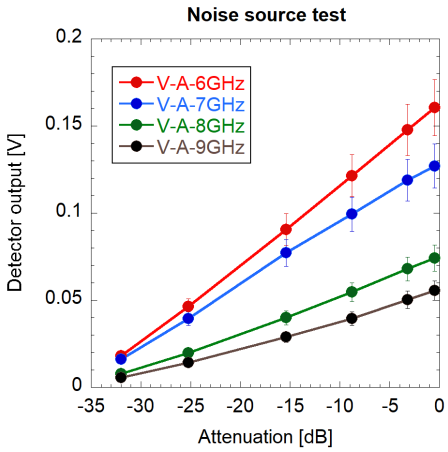

Fig. 10. Radiometer integrated test results with a noise source. Change in signal strength from the filter bank when the RF input signal to the mixer was controlled by adjusting the attenuator to vary the strength of the input signal from the noise source. V-A-6, 7, 8, and 9 GHz correspond to BPFs at 54, 55, 56, and 57 GHz, respectively.

3 Experimental Observations in LHD

This radiometer is designed for application to plasma experiments under magnetic field conditions from the magnetic field strength of B_t = 1 T to around 1.375 T. As shown in Figure 11, in the so-called inward-shifted configuration with the major radius at the magnetic axis of R_{ax} = 3.60 m, almost the entire region is observable at B_t = 1 T and 1.2 T, and even at 1.375 T, so is the region with the normalized small radius ρ > 0.5~~ is observable~~. In the standard configuration with R_{ax} = 3.75 m, the entire region is observable at 1 T, and even at 1.375 T, the measurement is possible around the rational surface region with ι/2π = 0.5. Here, ι is the rotational transform.

Some observation examples in plasma experiments are shown below.

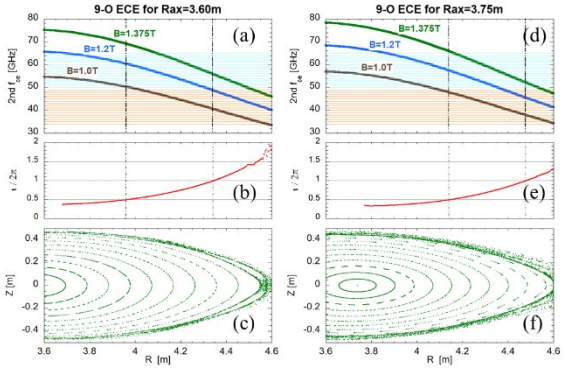

Fig. 11. (left) Radial distribution at Rax=3.60 m and (right) R_{ax} =3.75 m. (a, d) Second harmonic cyclotron frequencies at B_t =1 T, 1.2 T and 1.375 T. The orange and the light blue horizontal lines indicate the Q-~~band~~ and V-band measured channels' frequencies, respectively. (b, e) Iota distribution (c, f) Magnetic closed flux surfaces for every ρ =0.1.

NBI power modulation experiments were performed at the magnetic axis of R_{ax} =3.75 m and the magnetic field strength of B_t = 1.375 T. As shown in Figure 12(a), NBI4 and NBI5 which are perpendicular NBI beams were injected with power modulation from 3.4 s to 8.2 s. The time variation of the electron temperature T_e obtained with this radiometer is shown in Figure ~~11~~12(b). As can be seen from the figure, T_e oscillates significantly in sync with the power modulation. The radial profile of T_e measured by Thomson scattering of the OFF (green) and ON (red) timing of NBI power modulation is shown in Figure 13(a). Also shown are the fitted data of T_e profiles obtained from this data by fitting based on Bayesian statistics [17, 18]. It shows the difference in T_e due to modulation seems to be arisen the region around R=4.5m~~It is found that the difference in T_e due to modulation is arisen in the edge region~~. Figure 13(b) shows ~~a~~ time-expanded ECE radiometer data measured in this region, ~~showing~~ demonstrating that the phase difference between the R<4.51m region and ~~the region~~that outside the R>4.51m region is observed by ECE. In contrast to local heating by ECH, NBI heating is generally considered to affect a wider radial region from the outside of the plasma at the same time. The present measurements revealed that the heating of NBI may be accompanied by localized changes in the plasma. The ECE measurements also show a different response in the core region than the Thomson scattering measurements. Further analysis is needed to integrate and understand these results, and this is an issue for the future.~~In contrast to local heating by ECH, NBI heating is generally considered to affect a wider radial region from the outside of the plasma at the same time. The present measurements reveal that NBI heating can be accompanied by localized changes in the plasma.~~

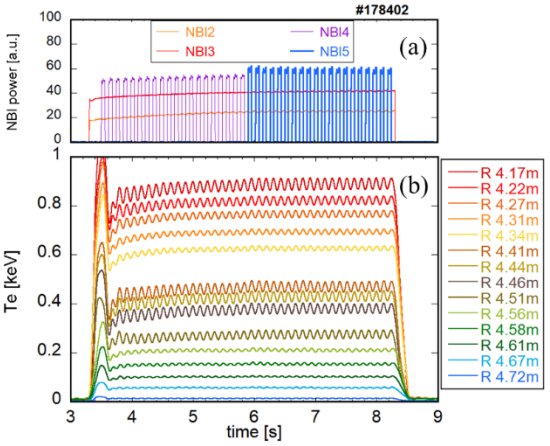

Fig. 12. Time variation observation of T_e in NBI power modulation experiments. (a) Incident modulated power of the four NBIs and (b) time variation of the converted signal intensity T_e at each radial position of the ECE.

~~Radiometer~~ The radiometer is also expected to observe MHD fluctuations such as Alfvén eigenmodes and electrostatic oscillations. Figure 14 shows an example of the frequency spectrum of the radiometer signal when these oscillations are generated. Comparing the signal strength before the plasma discharge as a noise level, the signal was found to be about one order of magnitude stronger during the discharge. In particular, modes identified as frequency chirp-up reversed shear Alfvén eigenmode (RSAE), geodesic acoustic mode (GAM) ~~(RSAE), GAM~~ oscillations around 20 kHz [19, 20] and these higher harmonics ~~are~~ were successfully observed. Since we can now obtain information on various types of temperature fluctuations, we expect to be able to use this information to study their spatial structure and interactions in the future.

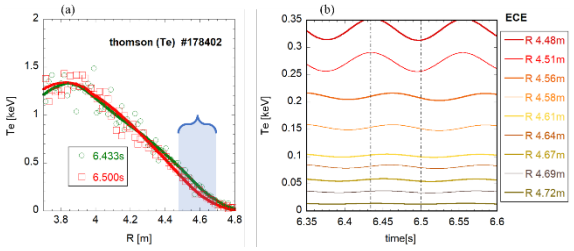

Fig. 13. (a) T_e radial profiles measured by Thomson scattering. Green and red solid lines are obtained by fitting. (b) Time variation of electron temperature obtained by ECE in the region shown in blue in (a).

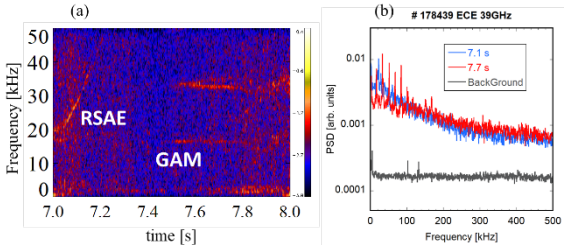

Fig. 14. Examples of RSAE and GAM oscillation observations. (a) Spectrogram, and (b) frequency spectra of two timings. The gray line is the estimated background noise for this channel.

4 Conclusion

A new ECE radiometer covering the Q and V bands has been developed. The purpose of this radiometer is to observe fluctuations and time variations of electron temperature in low magnetic field experiments at LHD. Due to the limitation of the available port and vacuum window, a focusing mirror designed by Gaussian beam optics was installed in the vacuum vessel for efficient ECE wave transmission. The beam width on the test bench is in good agreement with the estimated value with Gaussian beam propagation. The heterodyne radiometer uses a low-noise local oscillator and has a dynamic range of more than 30 dB when tested with a noise source. To remove the stray lights due to 56 and 77 GHz gyrotrons, a notch filter was created using an oversized waveguide, and more than 50 dB of attenuation was obtained. By implementing this ECE system ~~to~~ in LHD, oscillations due to NBI modulation of the radiated ECE waves from the plasma, Alfvén eigenmodes, and GAM oscillations were also successfully observed.

In addition, the LHD data can be accessed from the LHD data repository at https://www-lhd.nifs.ac.jp/pub/Repository_en.html.

Acknowledgments

The authors are grateful to the LHD experiment group for the excellent operation of the device. This work was partially supported ~~in part~~ by KAKENHI (Nos. 21H04973 and 19H01880), by a budgetary Grant-in-Aid from the NIFS LHD project, under the auspices of the NIFS Collaboration Research Program (NIFS22ULPP051 and NIFS22KBAP065).

References

1. A. Iiyoshi et al., Nucl. Fusion **39**, 1245 (1999).
2. Y. Takeiri et al., Nucl. Fusion **57**, 102023 (2017).
3. Y. Nagayama et al., Rev. Sci. Instrum. **70**, 1021 (1999).
4. P. C. de Vries et al., Phys. Plasmas, **7**, 3707 (2000).
5. H. Sasao et al., Fusion Engineering and Design **53**, 153 (2001).
6. Y. Nagayama et al., Fusion Eng. Des., **53**, 201 (2001).
7. K. Kawahata et al., Rev. Sci. Instrum., **72**, 387 (2001).
8. K. Kawahata et al., Rev. Sci. Instrum., **74**, 1449 (2003).
9. Y. Nagayama et al., IEEE Trans. Plasma Sci., **32**, 1716 (2004).
10. T. Tokuzawa et al., Fusion Science and Tech. **58**, 364 (2010).
11. H. Tsuchiya et al., Plasma and Fusion Research, **6**, 2402114 (2011).
12. S. Sakakibara, et al., Nucl. Fusion **57**, 066007 (2017).
13. Y. Suzuki et al., “Improved particle confinement in the L-H transition in the 3D magnetic field”, 5th Asia-Pacific Conference on Plasma Physics, 26 Sept-1 Oct, (2021).
14. Wenqing HU et al., Plasma and Fusion Research, **6**, 2402031 (2021).
15. J. Varela et al., Nucl. Fusion **60**, 046013 (2020).
16. M. Nishiura et al., Rev. Sci. Instrum. **92**, 034711 (2021).
17. K. Fujii et al., Rev. Sci. Instrum. **88**, 013508 (2017).
18. K. Fujii et al., IEEE Trans. Plasma Sci. **47**, 3305 (2019).
19. K. Toi et al., Phys. Rev. Lett. **105**, 145003 (2010).
20. T. Ido et al., Nucl. Fusion **51** 073046 (2011).